Hindawi
Shock and Vibration
Volume 2020, Article ID 2747204, 20 pages
https://doi.org/10.1155/2020/2747204

Research Article

Investigation of Nonlinear Characteristics of a Gear Transmission System in a Braiding Machine with Multiple Excitation Factors

Lingling Yao, Zhuo Meng, Jianqiu Bu, and Yize Sun

College of Mechanical Engineering, Donghua University, Shanghai 201620, China

Correspondence should be addressed to Zhuo Meng; mz@dhu.edu.cn

Received 24 May 2019; Revised 27 November 2019; Accepted 23 January 2020; Published 25 March 2020

Academic Editor: Juan C. G. Prada

Copyright © 2020 Lingling Yao et al. This is an open access article distributed under the Creative Commons Attribution License, which permits unrestricted use, distribution, and reproduction in any medium, provided the original work is properly cited.

In this study, we attempt to analyze the influence of different excitation factors on the dynamic behavior of a gear transmission system in a braiding machine. In order to observe nonlinear characteristics, a mathematical model is established with a six-degrees-of-freedom gear system for consideration of multiple excitation factors. Iterative results are used to study the nonlinear characteristics of the gear system with respect to contact temperature, varying levels of friction, and disturbance of yarn tension using bifurcation diagrams, maximum Lyapunov exponents, phase diagrams, Poincare maps, and the power spectrum. The numerical results show that excitation factors such as temperature and surface friction, among others, have considerable influence on the nonlinear characteristics of the gear system in a braiding machine, and the model is evaluated to show the key regions of sensitivity. The analysis of associated parameters can be helpful in the design and control of braiding machines.

1. Introduction

Braiding is a traditional technique used in textile production. In recent years, the emergence of new materials and different types of braiding machines has led to an upsurge in research on braiding.

Most of the studies of 3-D braided composites focus on the braiding process, structure, parameters, and performance analysis of composite materials. Ma et al. [1] proposed a mathematical model of tension versus yarn displacement, and Guyader et al. [2] analyzed the relationships between the process parameters and the geometry of the braid. Hajrasouliha et al. [3] presented a theoretical model for the prediction of braid angle at any point of a mandrel with constant arbitrary cross section by considering the kinematic parameters of a circular braiding machine. Shen and Branscomb [4] proposed a purely mathematical model to generate the 3D geometry of braided structures, and Wehrkamp-Richter et al. [5] studied the damage and failure characteristics of triaxial braided composites. Swery et al. [6] provided a complete simulation process for predictions on the manufacturing of braided composite parts. However, further research holds the promise of improving the performance of 3-D circular braiding machines. Zhang et al. [7] proposed that the performance of a braiding machine depends on the motion system, and the key component of the motion system is the gear system. The dynamic excitation created by the gear transmission system in a braiding machine is the main source of vibrations, and these nonlinear vibrations reduce braid quality and have become an issue of urgent concern.

Gear transmissions are widely used in engineering machinery, ocean engineering, traffic and transportation, metallurgy, and building materials, and they exhibit a long life span, smooth operation, high load capacity, and high reliability. There has been considerable research on gear systems since 1990, and one of the main goals is the development of dynamic models. Dynamic modeling methods include the lumped parameter method, the finite element method, the lumped mass method, the transfer matrix method, and the power bond graph method. In 1990, Kahraman and Singh [8] established a nonlinear dynamic model for a single-stage gear system by considering error and backlash. Later, these same authors [9] established a nonlinear dynamic model of a 3DOF gear system that considers comprehensive transmission error, backlash, time-varying meshing stiffness, and bearing

clearance. Vaishya and Singh [10] established a gear dynamic model with time-varying friction, and Luo [11] established a gear dynamic model considering friction, collision, and lubrication condition. He et al. [12] developed a single-stage gear dynamic model considering friction and time-varying meshing stiffness, and Liu and Parker [13] proposed a multiple-stage gear dynamic model considering contact looseness, load fluctuation, and tooth profile modification. Chang-Jian [14] developed a model considering nonlinear oil film force, nonlinear support, and nonlinear meshing force, Li and Kahraman [15] considered transient elastohydrodynamic lubrication, and Huang et al. [16] considered variable lubricating oil damping. Eritenel and Parker [17] established the equivalent stiffness model in 2012, and Cui et al. [18] established a gear-rotor dynamic model considering nonlinear meshing force and nonlinear oil film force, while Chen et al. [19] established a gear dynamic model considering backlash and asymmetric meshing stiffness. Baguet and Jacquenot [20] established a gear-rotor-bearing coupling dynamic model considering nonlinear support and nonlinear meshing stiffness, Li and Kahraman [21] established a friction dynamic model considering lateral torsion and hybrid elastohydrodynamic lubrication, and Wei [22] developed a multiple-degree-of-freedom gear dynamic model for high-speed locomotives by considering bearing clearance, backlash, and time-varying meshing stiffness. Gao et al. [23] considered transmission error, time-varying meshing stiffness, backlash, nonlinear oil film force, and gear meshing force, and Zhang [24] established a gear-rotor dynamic model considering backlash and radial clearance. Xiang-Feng [25] established a single-degree-of-freedom torsion-vibration model considering the temperature of the tooth surface, and Zhang [26] investigated the influence of multiple excitation factors operating on the dynamic characteristics of a gear system, including time-varying friction, transmission error, and backlash. This literature review shows that various excitation factors have been considered in modeling equations for gear systems, and these can realize close correspondence to actual working conditions.

It is clear that contact temperature, time-varying friction, and transmission error cannot be ignored when modeling the gear transmission system. To the authors' knowledge, studies on nonlinear dynamic features of gear transmission systems for 3-D circular braiding machines are scarce. Zhang et al. [7] researched nonlinear dynamic characteristics of gear transmission systems in braiding machines and considered disturbance of yarn tension and transmission error, but not contact temperature or time-varying friction. However, contact temperature and time-varying friction have an important influence on the dynamic behavior of a gear transmission system in a braiding machine. In this paper, we analyze nonlinear dynamic characteristics of a gear transmission system in a braiding machine and consider disturbance of yarn tension, transmission error, time-varying friction, and contact temperature; all of these factors are of potential importance in the development of models to improve braiding quality, and the associated parameters will be helpful in the design and control of braiding machines.

2. Dynamic Modeling

2.1. Braiding Process. To gain a better understanding of the braiding process, a schematic of a radial braiding machine with an industrial robot is shown in Figure 1. The radial braiding machine has 88 horn gears, each of which has four slots. The carriers are installed with the 1F1E arrangement (a gap is set between two adjacent carriers in the same group) and 176 carriers are driven during the braiding process. The radial braiding machine has 1 layer and 176 spindles, as is established with the coordinate system shown in Figure 1; the rotational center of the end of the robot effector is the origin, and the X, Y, and Z axes are as shown. F_{ij} refers to the force that yarn of the ith ($i = 1, 2, \ldots, n$) spindle on the jth ($j = 1, 2, \ldots, m$) track exerts on the mandrel, and this can be obtained from the actual situation; α refers to the angle between one yarn and the Z-axis; ω refers to the angular velocity of the spindle; ϕ_{ij} refers to the angle between one yarn and the horizontal plane as projected in the X-Y plane. Half of the carriers move in a clockwise direction, while the other half move in a counterclockwise direction during the braiding process. As shown in Figure 2, the carriers in the CA group move counterclockwise, and the carriers in the CB group move clockwise. Meanwhile, the traction system drags the robot with the mandrel, which causes the mandrel to move along the braiding center.

2.2. Dynamic Modeling of the Gear System. Figures 3(a) and 3(b) show that the transmission chain of a radial braiding machine consists of many transmission structures, including the transmission shaft, bearing, horn gear, gear, woodruff key, carrier, and shaft sleeve. Obviously, one crucial structure of the motion system in a radial braiding machine is the gear. Optimizing gear meshing to minimize vibration is an effective way of improving the performance of the braiding machine.

To aid the consideration of the nonlinear characteristics of the motion system in a radial braiding machine, a schematic illustration is shown in Figure 4 and the dynamic equations of the gear system areas are established in equation (1). Here, m_p and m_g are the masses of the gears; m_e is the effective mass; c_{px}, c_{py}, c_{gx}, and c_{gy} are the equivalent dampings of bearing; δ_{px} is the random disturbance of c_{px}; δ_{py} is the random disturbance of c_{py}; δ_{gx} is the random disturbance of c_{gx}; δ_{gy} is the random disturbance of c_{gy}; k_{px}, k_{py}, k_{gx}, and k_{gy} are the equivalent stiffnesses of bearings; f_{px}, f_{py}, f_{gx}, f_{gy}, and $f_h$are the displacement functions of the bearing; Λ is the sign function; $F(t)$ represents friction at the tooth surface; F_{px}, F_{py}, F_{gx}, and F_{gy} are the forces transmitted from the bearing; F_{e1} and F_{e2} are the eccentric forces; φ_p and $\varphi_g$are the angular displacements of the gear; $\phi_p(\tau)$ and $\phi_g(\tau)$ are the phase angles of eccentric force; c_h is the damping coefficient of gear meshing; δ_{ch} is the random

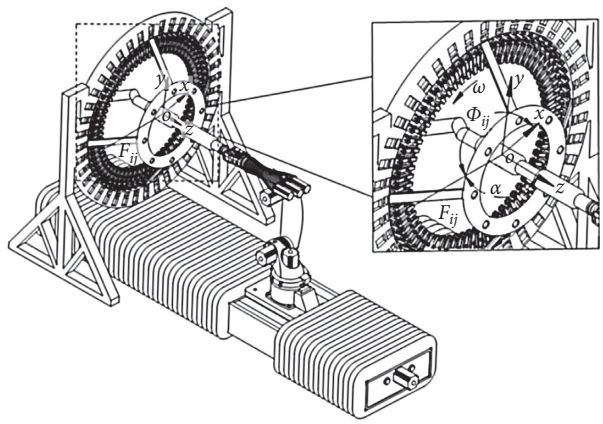

Figure 1: Diagram of the mandrel dragged by the robot in a three-dimensional braiding machine.

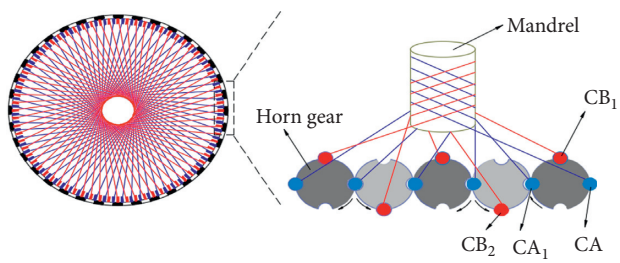

Figure 2: Diagram of the braiding process.

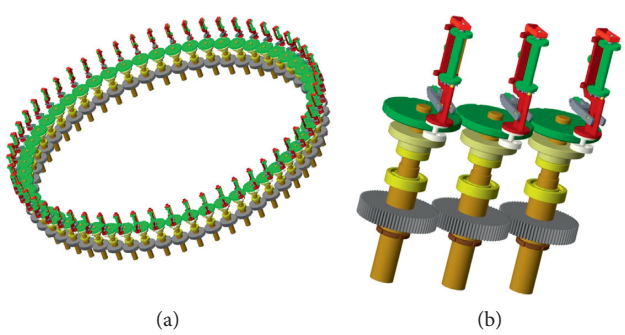

Figure 3: (a) Diagram of a closed-loop gear transmission system in a 3-D circular braiding machine gear transmission system. (b) Partial diagram of the gear transmission system.

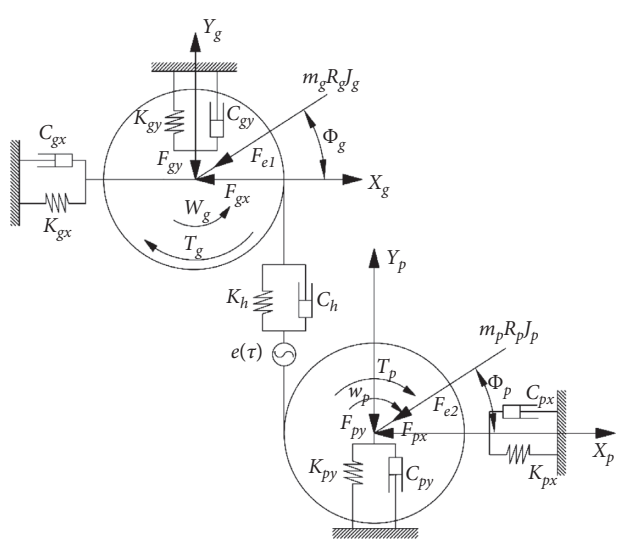

Figure 4: Dynamic model of gear transmission system.

disturbance of c_h; R_p and R_g are the base circle radii of the gear; x_p, x_g, y_p, and y_g are the center displacements of gears; $e(\tau)$ is the static transmission error; $k_h(\tau)$ is the time-varying meshing stiffness coefficient; J_p is the rotational inertia of the initiative gear; T_p is the driving torque of the initiative gear; J_g is the rotational inertia of the passive gear; ρ_p and ρ_g are the masses of eccentric arms; ω_p and ω_g are the angular velocities of gears; T_g is the load torque of the passive gear; δ is the relative torsional displacement of gear pairs; k_w is the amplitude of the time-varying stiffness fluctuation caused by temperature variation; δ_F is the random disturbance of load. In order to describe the meshing position and state accurately, a schematic diagram of the spread angle of active gears is shown in Figure 5.

The dynamic equations of a gear transmission system in a radial braiding machine are established according to Newton's laws as follows:

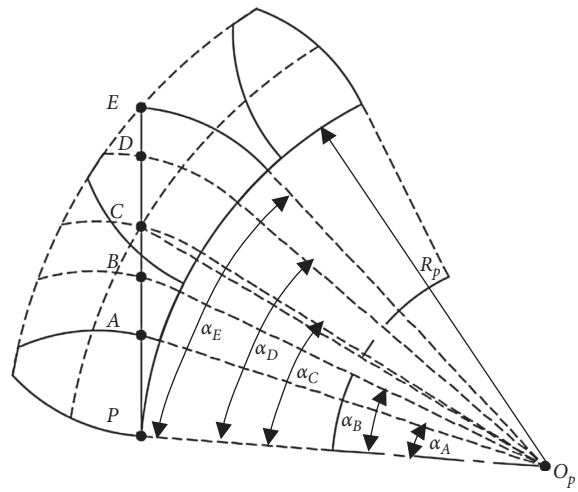

Figure 5: Schematic diagram of spread angle of initiative gear.

$$\begin{cases} m_p \cdot x_p + \left(c_{px} + \delta_{px}\right) \cdot \ddot{x}_p + k_{px} \cdot f_{px}\left(x_p\right) - \sum_{i=1}^{n} \Lambda_i F_i(t) + F_{px} + F_{e1} \cdot \cos\left[\phi_p(\tau)\right] = 0, \\ m_p \cdot y_p + \left(c_{py} + \delta_{py}\right) \cdot \ddot{y}_p + k_{py} \cdot f_{py}\left(y_p\right) + \left(c_h + \delta_{ch}\right) \cdot \left[R_p \cdot \ddot{\theta}_p - R_g \cdot \ddot{\theta}_g + \ddot{y}_p - \ddot{y}_g - \ddot{e}(\tau)\right] + \ldots \\ k_h(\tau) \cdot f_h\left[R_p \cdot \theta_p - R_g \cdot \theta_g + y_p - y_g - e(\tau)\right] + F_{py} + F_{e1} \cdot \sin\left[\phi_p(\tau)\right] = 0, \\ J_p \cdot \theta_p + R_p \cdot \left(c_h + \delta_{ch}\right) \cdot \left[R_p \cdot \ddot{\theta}_p - R_g \cdot \ddot{\theta}_g + \ddot{y}_p - \ddot{y}_g - \dot{e}(\tau)\right] + \ldots \\ R_p \cdot k_h(\tau) \cdot \left[R_p \cdot \theta_p - R_g \cdot \theta_g + y_p - y_g - e(\tau)\right] = T_p + \sum_{i=1}^{n} \Lambda_i R_{pi}(t) F_i(t) + \delta_F, \\ m_g \cdot x_g + \left(c_{gx} + \delta_{gx}\right) \cdot \ddot{x}_g + k_{gx} \cdot f_{gx}\left(x_g\right) + \sum_{i=1}^{n} \Lambda_i F_i(t) - F_{gx} - F_{e2} \cdot \cos\left[\phi_g(\tau)\right] = 0, \\ m_g \cdot y_g + \left(c_{gy} + \delta_{gy}\right) \cdot \ddot{y}_g + k_{gy} \cdot f_{gy}\left(y_g\right) - \left(c_h + \delta_{ch}\right) \cdot \left[R_p \cdot \ddot{\theta}_p - R_g \cdot \ddot{\theta}_g + \ddot{y}_p - \ddot{y}_g - \ddot{e}(\tau)\right] - \ldots \\ k_h(\tau) \cdot f_h\left[R_p \cdot \theta_p - R_g \cdot \theta_g + y_p - y_g - e(\tau)\right] - F_{gy} - F_{e2} \cdot \sin\left[\phi_g(\tau)\right] = 0, \\ J_g \cdot \theta_g - R_g \cdot \left(c_h + \delta_{ch}\right) \cdot \left[R_p \cdot \ddot{\theta}_p - R_g \cdot \ddot{\theta}_g + \ddot{y}_p - \ddot{y}_g - \ddot{e}(\tau)\right] - \ldots \\ R_g \cdot k_h(\tau) \cdot \left[R_p \cdot \theta_p - R_g \cdot \theta_g + y_p - y_g - e(\tau)\right] = -T_g - \sum_{i=1}^{n} \Lambda_i R_{gi}(t) F_i(t) + \delta_F, \end{cases} \tag{1}$$

$$\begin{gathered} \delta = R_p \cdot \theta_p - R_g \cdot \theta_g + y_p - y_g - e(\tau), \\ m_e = \frac{J_p \cdot J_g}{J_p \cdot R_g^2 + J_g \cdot R_g^2}, \\ f_{px}(u), f_{py}(u), f_{gx}(u), f_{gy}(u), f_h(u) = \begin{cases} u - b, & u > b, \\ 0, & -b \le u \le b, \\ u + b, & u < -b, \end{cases} \quad u = y_p, y_g, x_p, x_g, \delta, \\ F_{e1} = m_p \cdot \rho_p \cdot \omega_p^2, \\ F_{e2} = m_g \cdot \rho_g \cdot \omega_g^2. \end{gathered} \tag{2}$$

After Fourier series expansion, we take the first-order components of $k_h(\tau)$ and $e(\tau)$, which are simplified as follows:

$$k_h(\tau) = k_0 + k_v \cos\left[\left(\omega_h + \delta_{\omega_h}\right)\tau\right], \tag{3}$$

$$e(\tau) = e_v \sin(\omega_h \tau). \tag{4}$$

Here, k_0 is the average meshing stiffness; k_v is the magnitude of variation of meshing stiffness; ω_h is the driving frequency of gear pairs; δ_{ω_h} is the random disturbance of ω_h; and e_v is the amplitude of transmission error.

The frequency of gear pairs is

$$\omega_n = \sqrt{\frac{k_0}{m_e}}. \tag{5a}$$

The frequency of gear p is

$$\omega_p = \sqrt{\frac{k_{py}}{m_p}}. \tag{5b}$$

The frequency of gear q is

$$\omega_g = \sqrt{\frac{k_{gy}}{m_g}}. \tag{5c}$$

The backlash ratio is

$$b^* = \frac{b}{b_c}. \tag{5d}$$

The stiffness ratio is

$$\varepsilon = \frac{k_{hv}}{k_{h0}}, \tag{5e}$$

where b is the actual backlash, b_c is the standard backlash, $b = b_c$, k_{hv} is the amplitude of time-varying meshing stiffness, and k_{h0} is the average stiffness.

2.3. Time-Varying Friction Coefficient and Calculation Model. The friction coefficient for a tooth surface is affected by many factors such as the micromorphology of the tooth surface, lubrication state, and meshing position. The predictive models of friction coefficient such as the Coulomb model and the smoothed Coulomb model are used to predict the friction coefficient of gears.

2.3.1. Coulomb Model. The Coulomb model is the simpler model. The friction coefficient does not change with the position of meshing contact point, and it can only change when the direction of friction is at a node:

$$f_{ci}(t) = S_{\text{avg}}\lambda(t) = S_{\text{avg}} \cdot \text{sign}\left((\alpha_C - \alpha_A) - \text{mod}\left(\Omega_p t, \alpha_D - \alpha_A\right)\right). \tag{6}$$

Here, S_{avg} is the prescribed friction coefficient, Ω_p satisfies $t = (\alpha_D - \alpha_A/\Omega_p)$, t is the time when the meshing point of the gear passes through a base pitch after meshing, $\alpha_A = 0.324$, $\alpha_B = 0.453$, $\alpha_C = 0.413$, $\alpha_D = 0.717$, and $\alpha_E = 0.845$, as shown below.

2.3.2. Smoothed Coulomb Model. Duan's [27] research shows that the time-varying friction coefficient has a functional relationship with the slip-rolling ratio. The relative slip rate near the node is infinitely close to zero. The Coulomb model needs to be smoothed as follows:

$$f_{si}(t) = \frac{2S_{\text{avg}}}{\pi}\arctan\left(\kappa \cdot x_i(t)\right) + x_i(t)\frac{2S_{\text{avg}}\sigma}{\pi\left[1 + \kappa^2 x_i^2(t)\right]}, \quad i = 1, 2, \tag{7}$$

where $x_i(t) = R_p((\alpha_C - \alpha_A) - \text{mod}(\Omega_p t, \alpha_D - \alpha_A))$, the smoothness, κ, is between 20 and 100, and σ is the overlap ratio.

For convenience in solving, a dimensionless transformation is made:

$$\left.\begin{array}{llll} t = \omega_n \tau & y_p^* = \dfrac{y_g}{b} & y_g^* = \dfrac{y_g}{b} & \alpha^* = \dfrac{\alpha}{b} \\ k_{b1x,y}^* = \dfrac{k_{b1x,y}}{b} & k_{b2x,y}^* = \dfrac{k_{b2x,y}}{b} & k_0^* = \dfrac{k_0}{b} & k_v^* = \dfrac{k_v}{b} \\ \omega_h^* = \dfrac{\omega_h}{\omega_n} & \omega_p^* = \dfrac{\omega_p}{\omega_n} & \omega_g^* = \dfrac{\omega_g}{\omega_n} & \end{array}\right\}. \tag{8}$$

For ease in programming, a variable substitution is made:

$$\left.\begin{array}{lllll} x_1 = y_p^* & x_2 = \dot{y}_p^* & x_3 = x_p^* & x_4 = \dot{x}_p^* & x_5 = y_g^* \\ x_6 = \dot{y}_g^* & x_7 = x_g^* & x_8 = \dot{x}_g^* & x_9 = \delta^* & x_{10} = \dot{\delta}^* \end{array}\right\}. \tag{9}$$

Substituting equations (2)–(9) into (1) gives

$$\dot{x}_1 = x_2, \tag{10}$$

$$\begin{aligned} \dot{x}_2 = {} & -2 \cdot \left(\gamma_{py} + \delta_{py}\right) \cdot x_2 - \eta_{py} \cdot f_{py}(x_1) - 2 \\ & \cdot \left(\gamma_{h1} + \delta_{ch1}\right) \cdot x_{10} - \ldots \eta_{11} \cdot f_h(x_9) - F_{py}^* \\ & - \rho_p^* \cdot \frac{\left(\omega_h^* + \delta_{\omega_h^*}\right)^2}{z_1} \cdot \sin\left[\frac{\left(\omega_h^* + \delta_{\omega_h^*}\right)t}{z_1}\right], \end{aligned} \tag{11}$$

$$\dot{x}_3 = x_4 \tag{12}$$

$$\begin{aligned} \dot{x}_4 = {} & -2 \cdot \left(\gamma_{px} + \delta_{px}\right) \cdot x_4 - \eta_{px} \cdot f_{px}(x_3) + F_1^*(t) \\ & - F_{px}^* - \rho_p^* \cdot \frac{\left(\omega_h^* + \delta_{\omega_h^*}\right)^2}{z_1^2} \cdot \cos\left[\frac{\left(\omega_h^* + \delta_{\omega_h^*}\right)t}{z_1}\right], \end{aligned} \tag{13}$$

$$\dot{x}_5 = x_6, \tag{14}$$

$$\dot{x}_6 = -2\cdot\left(\gamma_{gy}+\delta_{gy}\right)\cdot x_6 - \eta_{gy}\cdot f_{gy}(x_5) + 2 \cdot \left(\gamma_{h2}+\delta_{ch2}\right)\cdot x_{10} + \ldots \eta_{22}\cdot f_h(x_9) + F^*_{gy} + \rho^*_g \cdot \frac{\left(\omega^*_h+\delta_{\omega^*_h}\right)^2}{z_2^2}\cdot \sin\left[\frac{\left(\omega^*_h+\delta_{\omega^*_h}\right)t}{z_2}\right], \tag{15}$$

$$\dot{x}_7 = x_8, \tag{16}$$

$$\dot{x}_8 = -2\cdot\left(\gamma_{gx}+\delta_{gx}\right)\cdot x_8 - \eta_{gx}\cdot f_{gx}(x_7) - F^*_2(t) + F^*_{gx} + \rho^*_g \cdot \frac{\left(\omega^*_h+\delta_{\omega^*_h}\right)^2}{z_2^2}\cdot \cos\left[\frac{\left(\omega^*_h+\delta_{\omega^*_h}\right)t}{z_2}\right], \tag{17}$$

$$\dot{x}_9 = x_{10}, \tag{18}$$

$$\dot{x}_{10} = \dot{x}_2 - \dot{x}_6 - 2\cdot\left(\gamma_{h3}+\delta_{ch3}\right)\cdot x_{10} - \eta_{33}\cdot f_h(x_9) + F^*_0 + e^*_v\left(\omega^*_h+\delta_{\omega^*_h}\right)^2 \sin\left[\left(\omega^*_h+\delta_{\omega^*_h}\right)t\right] + \delta^*_F + F^*_3(t), \tag{19}$$

after dimensionless processing, and with z_1 and z_2 as the tooth numbers of the gear.

Here, $\gamma_{py} = (c_{py}/2\cdot m_p\cdot\omega_n)$, $\eta_{py} = (k_{py}/m_p\cdot\omega_n)$, $\gamma_{h1} = (c_h/2\cdot m_p\cdot\omega_n)$, $\eta_{11} = 1-(\varepsilon+\delta_\varepsilon)\cdot\cos[(\omega^*_h+\delta_{\omega^*_h})t + k_w]$, $F^*_{py} = (F_{py}/m_p\cdot b_c\cdot\omega_n^2)$, $\gamma_{px} = (c_{px}/2\cdot m_p\cdot\omega_n)$, $\eta_{px} = (k_{px}/m_p\cdot\omega_n)$, $F^*_1(t) = (\sum_{i=1}^n \Lambda_i\cdot F_i(t)/m_p\cdot b_c\cdot\omega_n^2)$, $F^*_2(t) = (\sum_{i=1}^n \Lambda_i\cdot F_i(t)/m_g\cdot b_c\cdot\omega_n^2)$, $F^*_{px} = (F_{px}/m_p\cdot b_c\cdot\omega_n^2)$, $\gamma_{gy} = (c_{gy}/2\cdot m_g\cdot\omega_n)$, $\eta_{gy} = (k_{gy}/m_g\cdot\omega_n)$, $\gamma_{h2} = (c_h/2\cdot m_g\cdot\omega_n)$, $\gamma_{h3} = (c_h/2\cdot m_e\cdot\omega_n)$, $\eta_{22} = 1-(\varepsilon+\delta_\varepsilon)\cdot\cos[(\omega^*_h+\delta_{\omega^*_h})t + k_w]$, $F^*_{gy} = (F_{gy}/m_g\cdot b_c\cdot\omega_n^2)$, $\gamma_{gx} = (c_{gx}/2\cdot m_g\cdot\omega_n)$, $\eta_{gx} = (k_{gx}/m_g\cdot\omega_n)$, $F^*_{gx} = (F_{gx}/m_g\cdot b_c\cdot\omega_n^2)$, $F^*_0 = (J_g\cdot R_p\cdot T_p\cdot + J_p\cdot R_g\cdot T_g/J_p\cdot J_g\cdot b_c\cdot\omega_n^2)$, $\eta_{33} = 1-(\varepsilon+\delta_\varepsilon)\cdot\cos[(\omega^*_h+\delta_{\varepsilon^*_h})t + k_w]$, and $F^*_3(t) = (\sum_{i=1}^n \Lambda_i\cdot F_i(t)/m_e\cdot b_c\cdot\omega_n^2)$.

3. Results and Discussion

Equations (10)–(19) are solved by iterative methods with step size $t = 0.05$, $z_1 = z_2 = 30$, $m_p = m_q = m_e = 0.456\,\text{kg}$, $J_p = J_q = 6\times10^{-6}\,\text{kg}\cdot\text{m}^2$, $b_c = 0.068\,\text{mm}$, $e_v = 0.034\,\text{mm}$, $k_0 = 2.23\times10^8 N/m$, $k_v = 1.12\times10^7 N/m$, $e^*_v = 0.05$, $F^*_{px} = 0.02$, $F^*_{py} = 0.2$, $F^*_{gy} = 0.2$, $F^*_{gy} = -0.2$, $\eta_{11} = 1.1$, $\eta_{22} = 1.1$, $\eta_{33} = 1.1$, $\gamma_{px} = 0.01$, $\gamma_{py} = 0.01$, $\gamma_{gx} = 0.01$, $\gamma_{gy} = 0.01$, $\gamma_{h1} = 0.012$, $\gamma_{h2} = 0.012$, $\gamma_{h3} = 0.05$, $\varepsilon = 0.18$, $\rho^*_p = 0.1$, $\rho^*_g = 0.1$, $F^*_0 = 0.15$, $\alpha_A = 0.324\,\text{rad}$, $\alpha_B = 0.453\,\text{rad}$, $\alpha_c = 0.413\,\text{rad}$, $\alpha_D = 0.717\,\text{rad}$, $\alpha_E = 0.845\,\text{rad}$, $R_p = R_g = 0.06\,\text{m}$, $S_{\text{avg}} = 0.991\,\mu\text{m}$, and initial conditions are as follows:

$$x_1(0) = 0, x_2(0) = -0.1, x_3(0) = 0, x_4(0) = -0.1, x_5(0) = 0, x_6(0) = -0.1, x_7(0) = 0, x_8(0) = -0.1, x_9(0) = 0, \text{ and } x_{10}(0) = -0.1.$$

3.1. Analysis of a System without Random Perturbation. The nonlinear characteristics of a radial braiding machine's gear transmission system without random perturbation are shown in Figures 6(a)–12. The vibrational bifurcation diagram of the system is presented in Figure 6(a), the maximum Lyapunov exponent diagram of the system is shown as Figure 6(b), and Poincare maps and corresponding phase trajectories of the system are shown in Figures 7–12.

The nonlinear vibration characteristics of the system and the relationship between ω and x_{10} are shown in Figure 6(a). Observations include the following:

(1) From Figure 6(a), the system has one periodic point when $\omega < 163.3$. The Poincare maps and corresponding phase trajectories of the system at $\omega = 110$ are shown in Figure 7, where it can be observed that the system converged rapidly to one periodic point at $\omega = 110$; this suggests that the system was stable.

(2) The system has four periodic points when $163.3 < \omega < 186.5$ and Poincare maps and corresponding phase trajectories of the system at $\omega = 170$ are shown in Figure 8.

(3) With the increase of ω, the number of periodic points changes when $186.5 < \omega < 190$.

(4) The system has nine periodic points when $190 < \omega < 213$, and Poincare maps and corresponding phase trajectories of the system at $\omega = 200$ are shown in Figure 9.

(5) From Figure 6(a), chaos occurs in the system when $213 < \omega < 240$. Poincare maps and corresponding phase trajectories of the system at $\omega = 232$ are shown in Figure 10.

(6) When $240 < \omega < 264.7$, the corresponding phase trajectories of the system comprise a limit cycle, and Poincare maps and corresponding phase trajectories of the system at $\omega = 243$ are shown in Figure 11.

(7) When $\omega < 264.7$, the system becomes divergent and uncontrollable, and Poincare maps and corresponding phase trajectories of the system at $\omega = 265$ are shown in Figure 12. Meanwhile, the maximum Lyapunov diagram of the system can also reflect the nonlinearity of the system to a certain extent, as is shown in Figure 6(b). The Lyapunov exponent is defined as $\lambda_k = \lim_{x\longrightarrow\infty}(1/i)\ln|\lambda_k^{(i)}|$, $k = 1, 2, \ldots, n$, where $|\lambda_1^i| \geq |\lambda_2^i| \geq \cdots \geq |\lambda_n^i|$. In Figure 6(b), the maximum Lyapunov exponent is negative or fluctuates near zero when $\omega < 213$, which indicates that the system is stable according to the Lyapunov theorem. The maximum Lyapunov exponent is positive when $\omega < 213$, which indicates that the system exhibits chaos and becomes divergent and uncontrollable.

The nonlinearity shown in Figure 6(b) is consistent with the analysis from Poincare maps and the corresponding phase trajectories of the system.

3.2. Systematic Analysis of k_w. The nonlinear characteristics of a gear transmission system as a function of k_w are analyzed in Figures 13(a)–20(b). The vibrational bifurcation diagram of the system with $k_w = 0.248$ is shown in Figure 13(a), the maximum Lyapunov diagram of the system

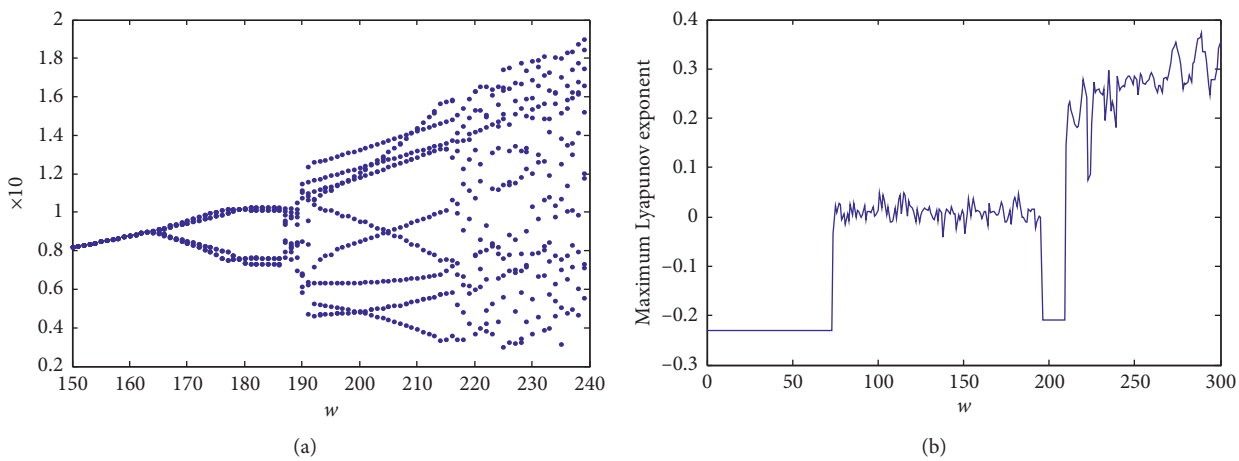

Figure 6: (a) Vibrational bifurcation diagram without perturbation. (b) Maximum Lyapunov exponent curve without perturbation.

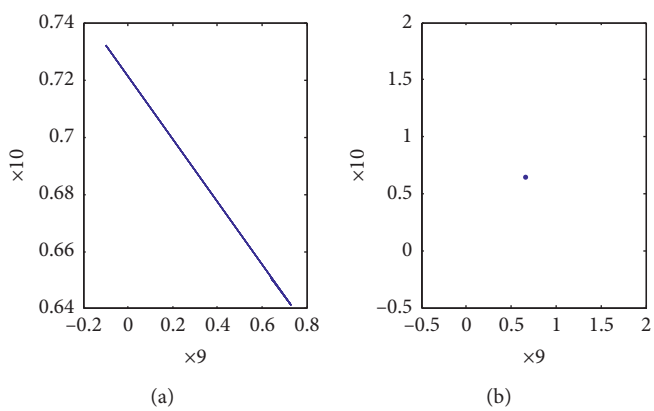

Figure 7: $\omega = 110$ without random perturbation. (a) Phase trajectories. (b) Poincare maps.

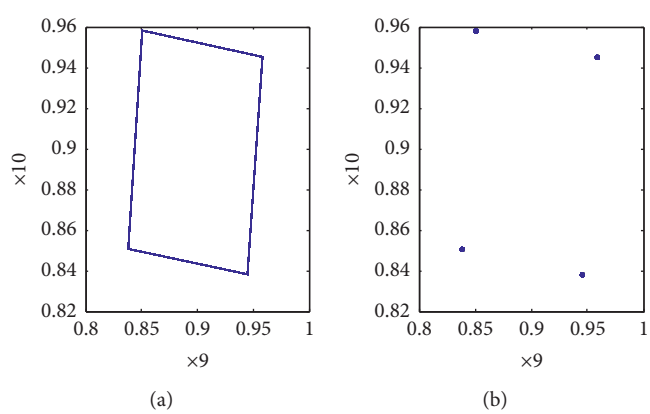

Figure 8: $\omega = 170$ without random perturbation. (a) Phase trajectories. (b) Poincare maps.

with $k_w = 0.248$ is shown in Figure 13(b), and Poincare maps and corresponding phase trajectories of the system with $k_w = 0.248$ are shown in Figures 14–19. In addition, the vibrational bifurcation diagram of a system with $k_w = 0.32$ is shown in Figure 20(a), and the maximum Lyapunov diagram of the system with $k_w = 0.32$ is shown in Figure 20(b). From Figures 13(a) and 20(a), it appears that k_w exerts a significant influence on the nonlinear characteristics of the gear transmission system. If k_w is relatively small, such as $k_w = 0.248$, there is a smaller influence on the nonlinear characteristics of the gear transmission system. The vibrational bifurcation diagram of the system, the maximum

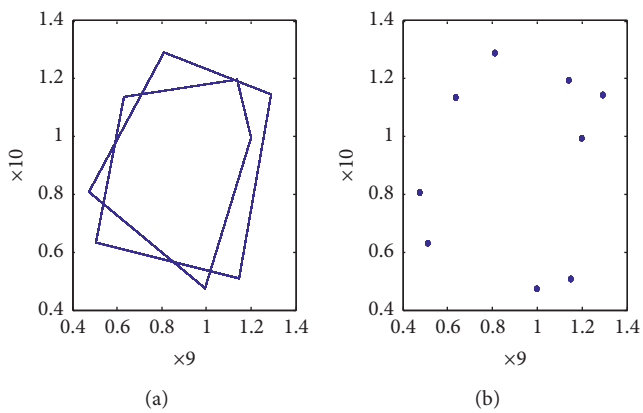

Figure 9: $\omega = 200$ without random perturbation. (a) Phase trajectories. (b) Poincare maps.

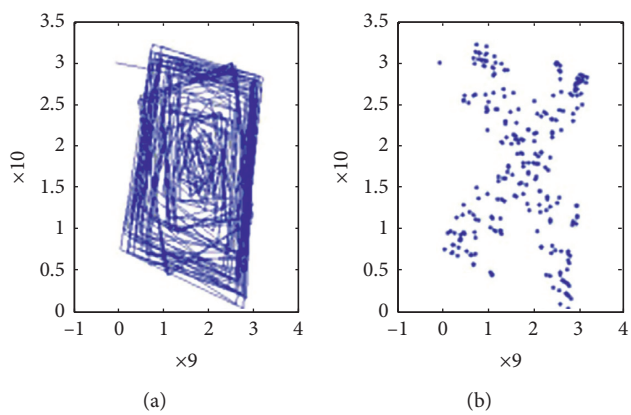

Figure 10: $\omega = 232$ without random perturbation. (a) Phase trajectories. (b) Poincare maps.

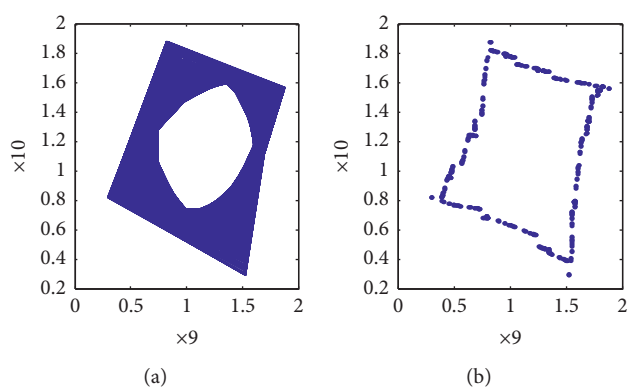

Figure 11: $\omega = 243$ without random perturbation. (a) Phase trajectories. (b) Poincare maps.

Lyapunov diagram of the system, and Poincare maps and corresponding phase trajectories of the system with $k_w = 0.248$ are shown in Figures 13(a)–19. Comparing Figures 6(a) and 13(a), it is observed that the vibration amplitude x_{10} when $k_w = 0.248$ is larger than the x_{10} resulting when $k_w = 0$, and the system exhibits chaos earlier when $k_w = 0.248$ as opposed to when $k_w = 0$. When $\omega = 200$, the system exhibits chaos with $k_w = 0.248$, but when $\omega = 213$, the system exhibits chaos with $k_w = 0$. When $\omega < 200$, the form of the solution with $k_w = 0.248$ is similar to that of $k_w = 0$. When $200 < \omega < 215$, the system exhibits chaos and Poincare maps and corresponding phase trajectories of the system at $\omega = 214$ are shown in Figure 17. When $215 < \omega < 240$, the corresponding phase trajectories of the system form a limit cycle. Poincare maps and corresponding phase trajectories of the system at $\omega = 234$ are shown in Figure 18. When $\omega = 240$, the system becomes divergent and uncontrollable. Poincare maps and corresponding phase

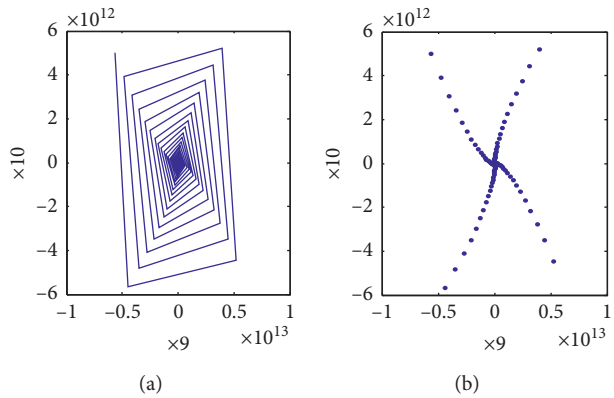

Figure 12: $\omega = 265$ without random perturbation. (a) Phase trajectories. (b) Poincare maps.

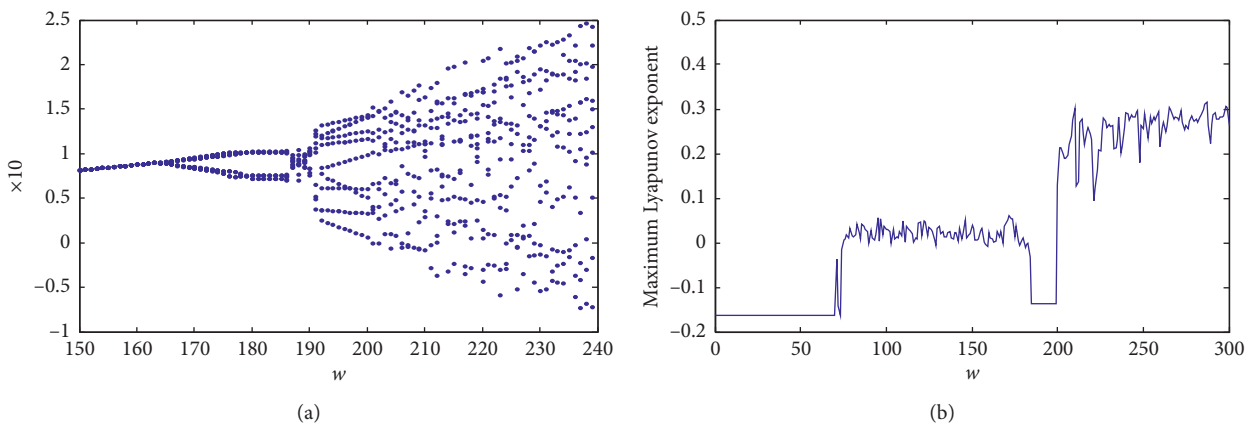

Figure 13: (a) Vibrational bifurcation diagram with $k_w = 0.248$. (b) Maximum Lyapunov exponent curve with $k_w = 0.248$.

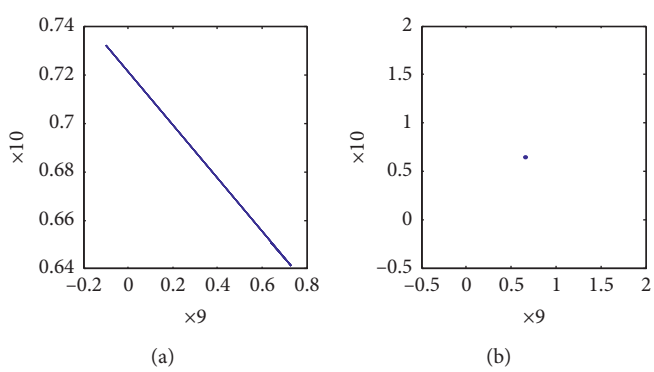

Figure 14: $\omega = 110$ and $k_w = 0.248$ without random perturbation. (a) Phase trajectories. (b) Poincare maps.

trajectories of the system at $\omega = 240$ are shown in Figure 19. From Figure 13(b), the maximum Lyapunov exponent is negative or fluctuates near zero when $\omega > 200$, indicating that the system is stable according to the Lyapunov theorem. The maximum Lyapunov exponent is positive when $\omega > 200$, indicating that the system exhibits chaos and becomes divergent and uncontrollable. The nonlinearity shown in Figure 13(b) is consistent with the analysis from Poincare maps and corresponding phase trajectories for the system. If k_w is relatively large, such as $k_w = 0.32$, there is a substantial influence on the nonlinear characteristics of the gear transmission system. The vibrational bifurcation diagram of the system, the maximum Lyapunov diagram of the system, Poincare maps, and corresponding phase trajectories of the system with $k_w = 0.32$ are shown in Figures 20(a) and 20(b). From Figure 20(b), it is clear that the maximum Lyapunov exponent is positive if k_w is relatively large, such as $k_w = 0.32$, indicating that the system exhibits chaos and

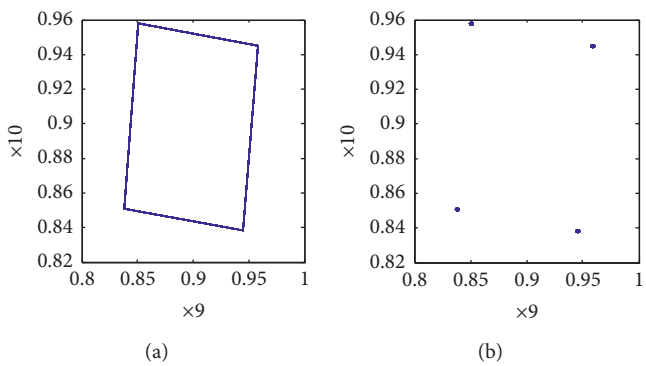

Figure 15: $\omega = 170$ and $k_w = 0.248$without random perturbation. (a) Phase trajectories. (b) Poincare maps.

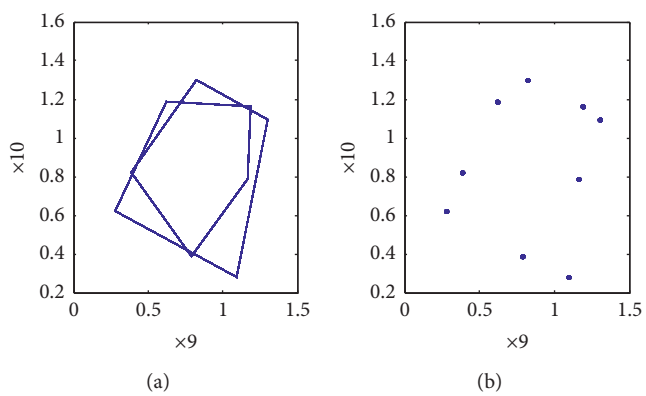

Figure 16: $\omega = 192$ and $k_w = 0.248$ without random perturbation. (a) Phase trajectories. (b) Poincare maps.

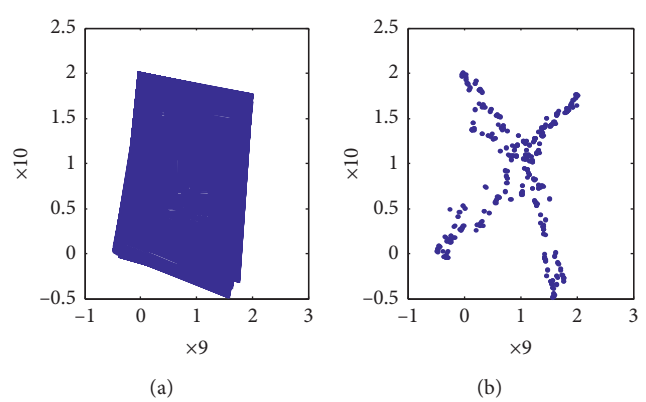

Figure 17: $\omega = 214$ and $k_w = 0.248$without random perturbation. (a) Phase trajectories, (b) Poincare maps.

becomes divergent and uncontrollable. Here, the Poincare maps and corresponding phase trajectories of the system are omitted.

3.3. Systematic Analysis of Friction on the Tooth Surface. The dynamic friction resulting from the Coulomb model is shown in Figure 21. Friction on the tooth surface exhibits an obvious periodic variation when $0.05 < t < 0.0581$ and

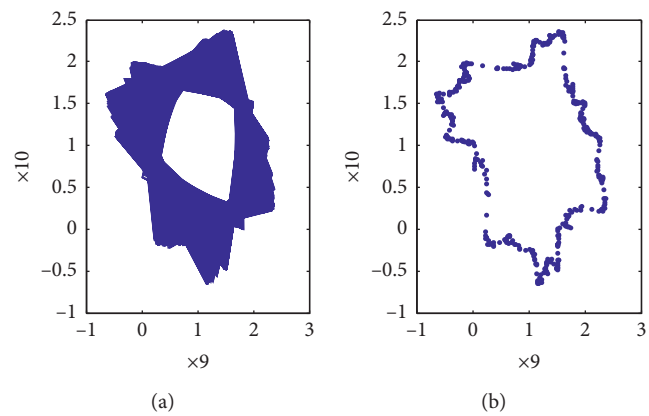

Figure 18: $\omega = 234$ and $k_w = 0.248$ without random perturbation. (a) Phase trajectories. (b) Poincare maps.

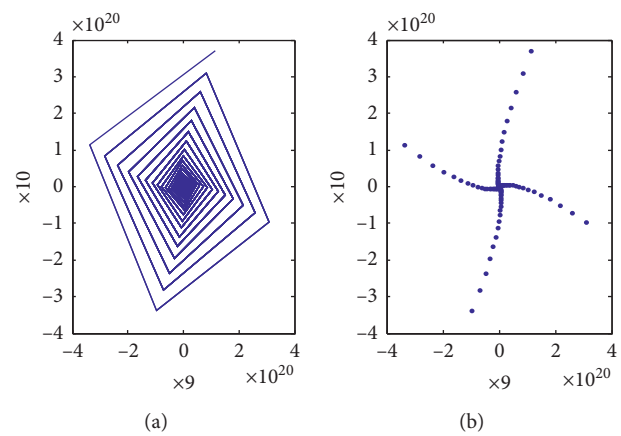

Figure 19: $\omega = 240$ and $k_w = 0.248$ without random perturbation. (a) Phase trajectories. (b) Poincare maps.

$\omega < 210$. Bifurcation diagrams, maximum Lyapunov exponents, phase diagrams, Poincare maps corresponding to Figure 21, and specific analyses are shown in Figures 22(a)–29. When $0.05 < t < 0.0581$, the vibrational bifurcation diagram for the system using the Coulomb model to predict the time-varying friction coefficient is shown in Figure 22(a); Figure 22(a) indicates that the nonlinear characteristics of friction on the tooth surfaces of the gear transmission system are complex. Observations include the following:

(1) When $0.05 < t < 0.0581$ and $\omega < 163.3$, the system has one periodic point. Poincare maps and corresponding phase trajectories of system at $\omega = 110$ are shown in Figure 23; this shows that the system rapidly converges to one periodic point, indicating that the system is stable.

(2) When $0.05 < t < 0.0581$ and $163.3 < \omega < 186.5$, the system has four periodic points, and Poincare maps and corresponding phase trajectories of system at $\omega = 174$ are shown in Figure 24.

(3) With increasing $\omega = 110$, the number of periodic points changes when $0.05 < t < 0.0581$ and $186.5 < \omega < 190$.

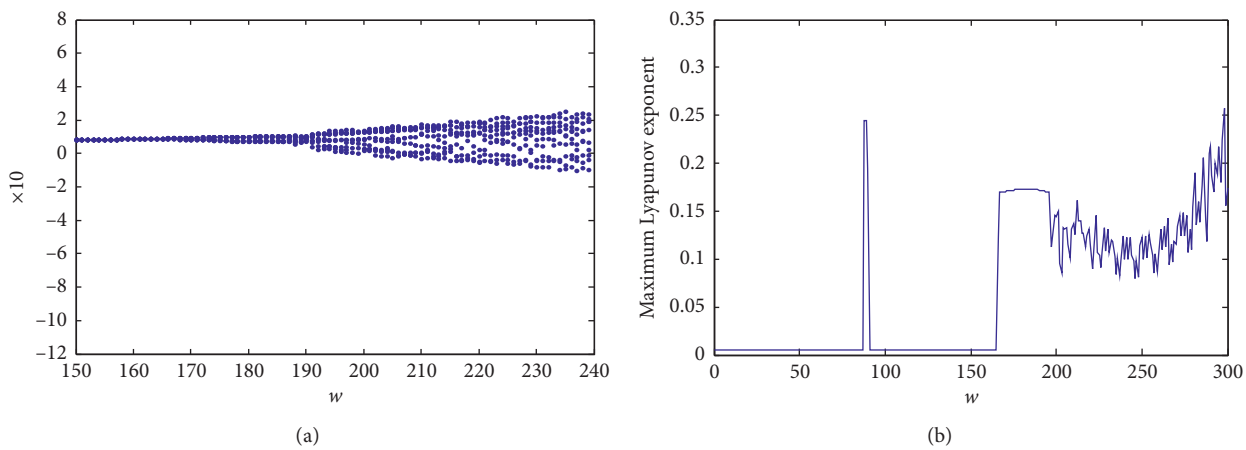

Figure 20: (a) Vibrational bifurcation diagram curve with $k_w = 0.32$. (b) Maximum Lyapunov exponent with $k_w = 0.32$.

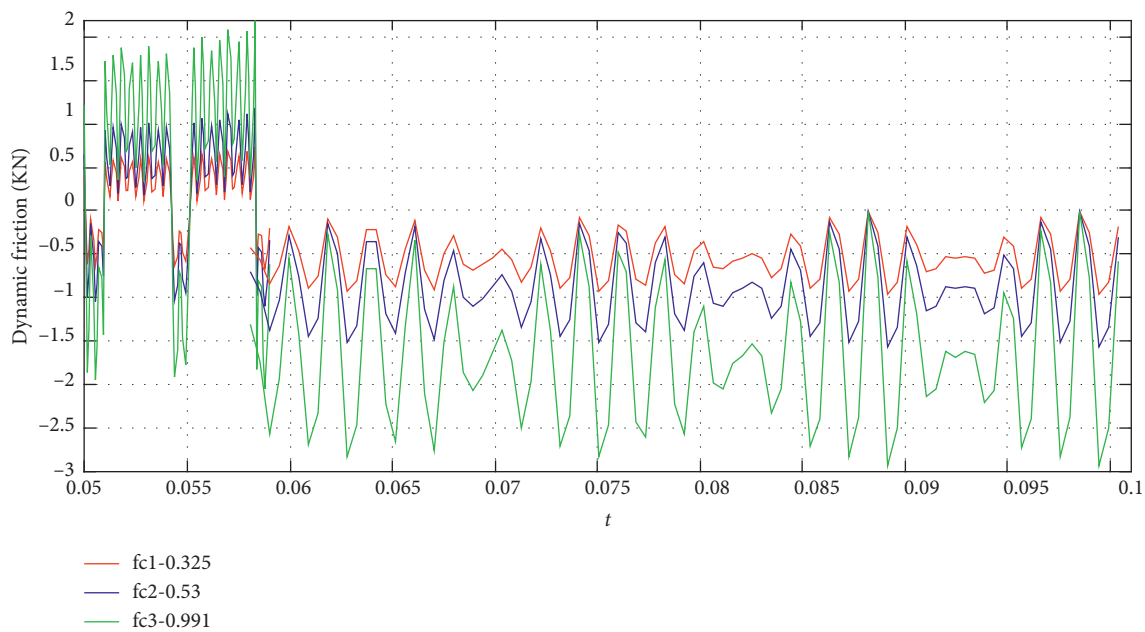

Figure 21: Dynamic friction with the Coulomb model.

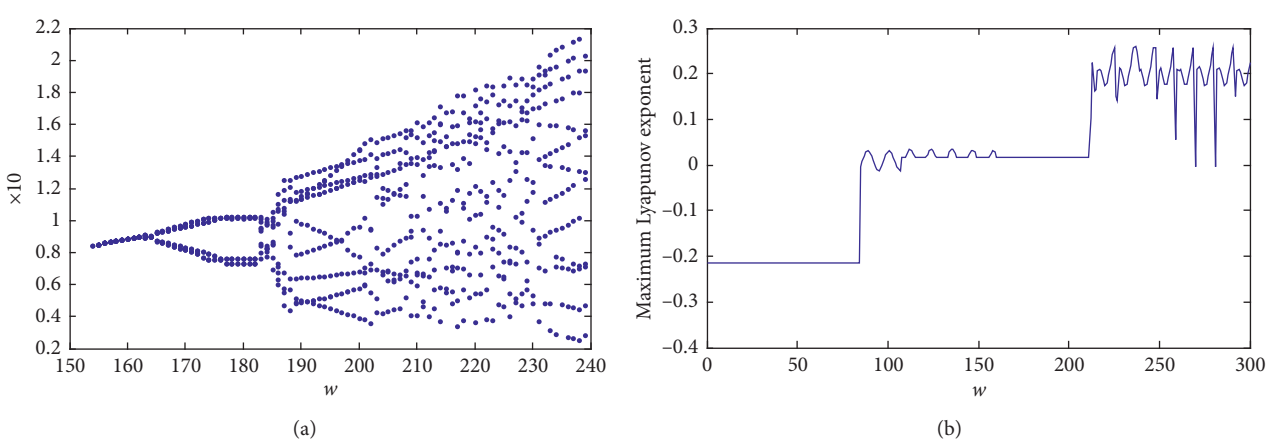

Figure 22: (a) Vibrational bifurcation diagram with the Coulomb model when $t \in [0.05 \;\; 0.0581]$. (b) Maximum Lyapunov exponent curve with the Coulomb model when $t \in [0.05 \; 0.0581]$.

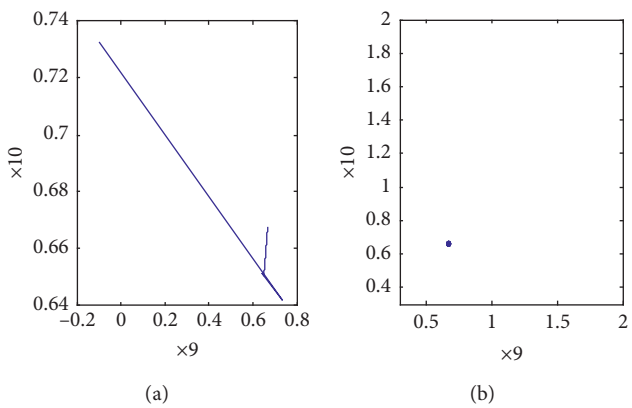

Figure 23: $\omega = 110$ and $k_w = 0$ with the Coulomb model when $t \in [0.05 \;\; 0.0581]$. (a) Phase trajectories. (b) Poincare maps.

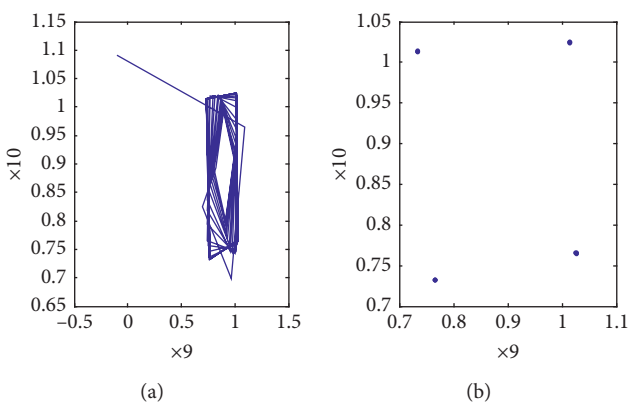

Figure 24: $\omega = 174$ and $k_w = 0$with the Coulomb model when $t \in [0.05 \;\; 0.0581]$. (a) Phase trajectories. (b) Poincare maps.

(4) When $0.05 < t < 0.0581$ and $190 < \omega < 203$, the system has nine periodic points, and Poincare maps and corresponding phase trajectories of the system at $\omega = 192$ are shown in Figure 25.

(5) From Figure 22(a), the system has a finite number of periodic points when $0.05 < t < 0.0581$ and $203 < \omega < 210$. Poincare maps and corresponding phase trajectories of the system at $\omega = 206$ are shown in Figure 26.

(6) From Figure 22(a), the phase trajectories of the system when $0.05 < t < 0.0581$ and $210 < \omega < 230$ constitute a limit cycle. Poincare maps and corresponding phase trajectories of the system at $\omega = 220$ are shown in Figure 27.

(7) When $230 < \omega < 272$, the system has 13 periodic points. Poincare maps and corresponding phase trajectories of the system at $\omega = 237$ are shown in Figure 28.

(8) When $\omega = 272$, the system becomes divergent and uncontrollable. Poincare maps and corresponding phase trajectories of the system at $\omega = 273$ are shown in Figure 29.

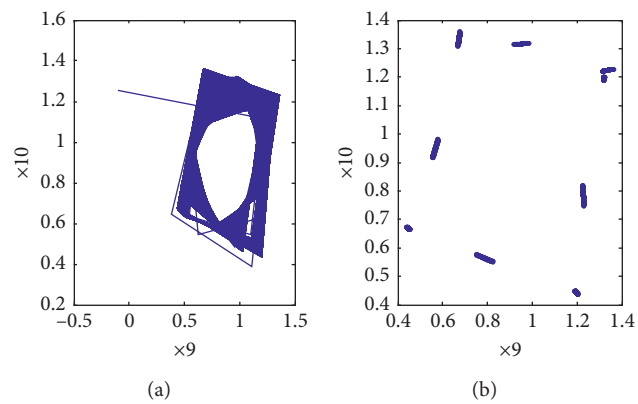

Figure 25: $\omega = 192$ and $k_w = 0$with the Coulomb model when $t \in [0.05 \;\; 0.0581]$. (a) Phase trajectories. (b) Poincare maps.

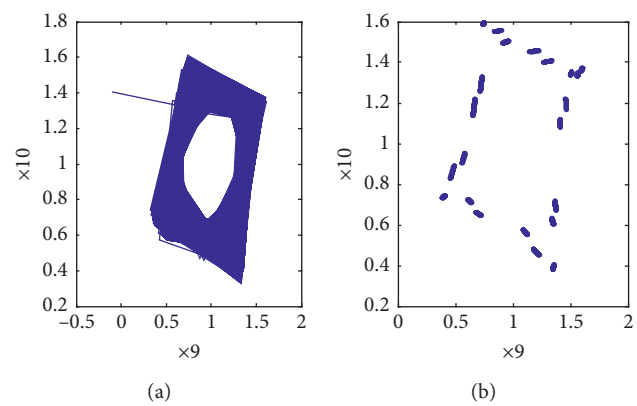

Figure 26: $\omega = 206$ and $k_w = 0$with the Coulomb model when $t \in [0.05 \;\; 0.0581]$. (a) Phase trajectories. (b) Poincare maps.

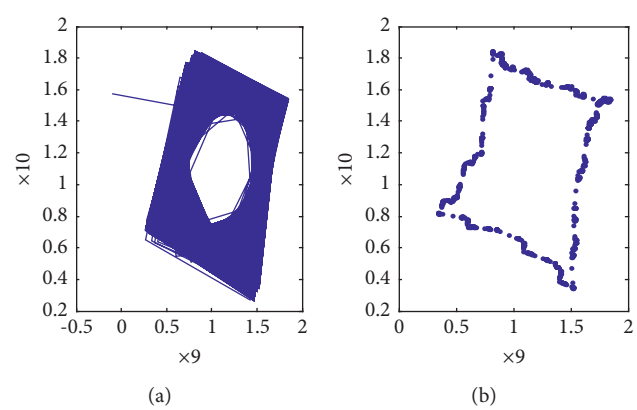

Figure 27: $\omega = 220$ and $k_w = 0$ with the Coulomb model when $t \in [0.05 \;\; 0.0581]$. (a) Phase trajectories. (b) Poincare maps.

From Figure 22(b), the maximum Lyapunov exponent is negative or fluctuates near zero when $\omega < 210$, indicating that the system is stable according to the Lyapunov theorem. The maximum Lyapunov exponent is positive when $\omega > 210$, which indicates that the system exhibits chaos and becomes divergent and uncontrollable. In general, friction in the

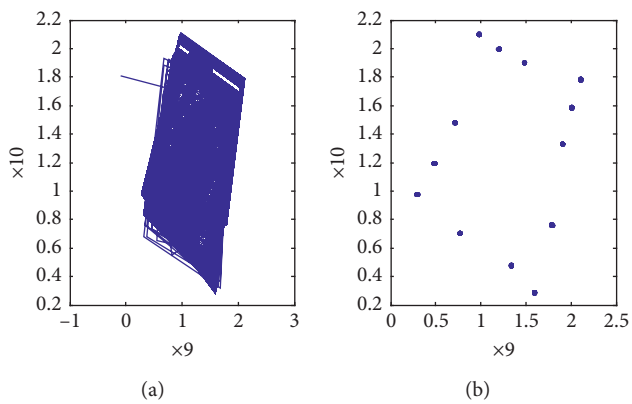

Figure 28: $\omega = 237$ and $k_w = 0$with the Coulomb model when $t \in [0.05 \;\; 0.0581]$. (a) Phase trajectories. (b) Poincare maps.

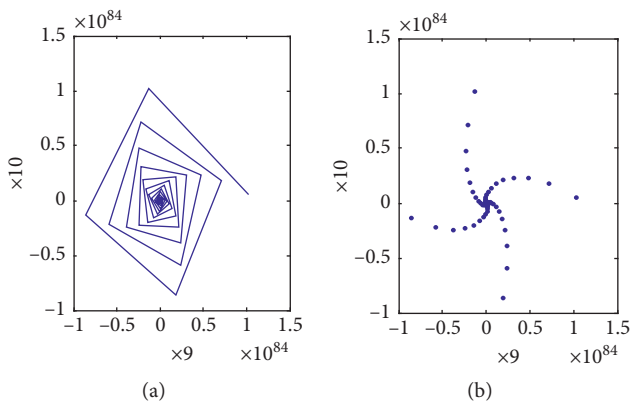

Figure 29: $\omega = 273$ and $k_w = 0$with the Coulomb model when $t \in [0.05 \;\; 0.0581]$. (a) Phase trajectories. (b) Poincare maps.

Coulomb model increases with an increase in tooth surface roughness because of the change in the nonlinear friction coefficient. Meanwhile, friction in the Coulomb model has nonperiodic and sharp fluctuations when $t > 0.0581$. Bifurcation diagrams, maximum Lyapunov exponents, phase diagrams, Poincare maps corresponding to Figure 21, and specific analyses are shown in Figures 30(a) and 30(b). When$t > 0.0581$, use of the Coulomb model to predict the time-varying friction coefficient exhibits chaos and becomes divergent and uncontrollable. Figure 30(a) shows the vibrational bifurcation diagram of the system using the Coulomb model to predict the time-varying friction coefficient when $0.0581 < t < 0.1009$, and the maximum Lyapunov diagram of the system is shown in Figure 30(b). From Figure 30(b), the maximum Lyapunov exponent is positive when $0.0581 < t < 0.1009$, which indicates that the system exhibits chaos and becomes divergent and uncontrollable. Here, the Poincare maps and corresponding phase trajectories of the system are omitted.

The dynamic friction obtained with the smoothed Coulomb model is shown in Figure 31. Friction on the tooth surface exhibits obvious periodic changes when $0.05 < t < 0.0597$ and $\omega < 201$. Bifurcation diagrams, maximum Lyapunov exponents, phase diagrams, Poincare maps corresponding to Figure 31, and specific analyses are shown in Figures 32(a)–38. The vibrational bifurcation diagram of the system using the smoothed Coulomb model to predict the time-varying friction coefficient when $0.05 < t < 0.0597$ is given in Figure 32(a), which shows that the nonlinear characteristics of tooth surface friction in the gear transmission system is complex. Observations include the following:

(1) When $0.05 < t < 0.0597$ and $\omega < 163.3$, the system has one periodic point. Poincare maps and corresponding phase trajectories of the system at $\omega = 110$ are shown in Figure 33. In Figure 33, the system rapidly converges to one periodic point, indicating that the system is stable.

(2) When $0.05 < t < 0.0597$ and $163.3 < \omega < 182$, the system has four periodic points. Poincare maps and corresponding phase trajectories of the system at $\omega = 174$ are shown in Figure 34.

(3) With the increase of ω, the number of periodic points changes when $0.05 < t < 0.0597$ and $182 < \omega < 190$.

(4) When $190 < \omega < 201$, the system has nine periodic points. Poincare maps and corresponding phase

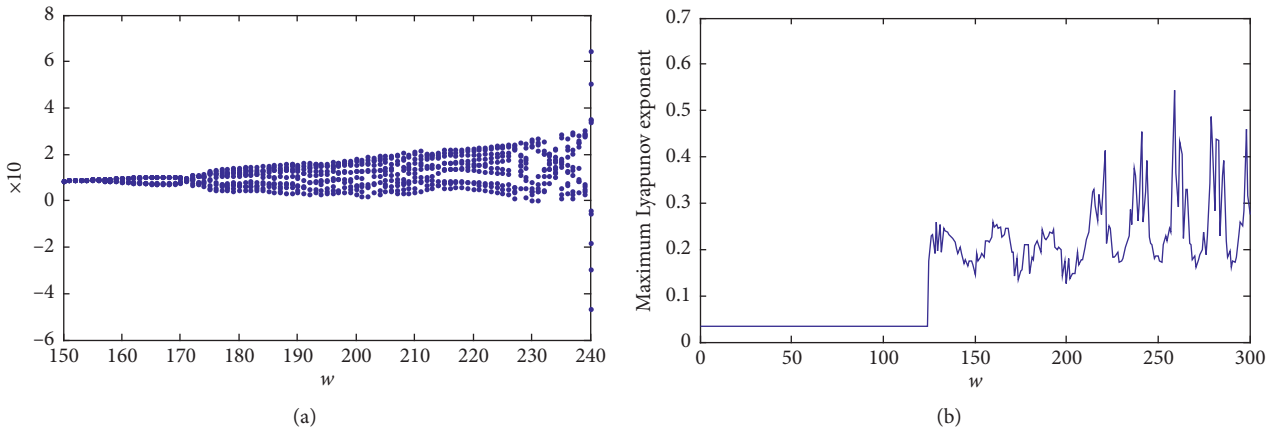

Figure 30: (a) Vibrational bifurcation diagram with the Coulomb model when $t \in [0.0581 \;\; 0.1009]$. (b) Maximum Lyapunov exponent curve with the Coulomb model when $t \in [0.0581 \;\; 0.1009]$.

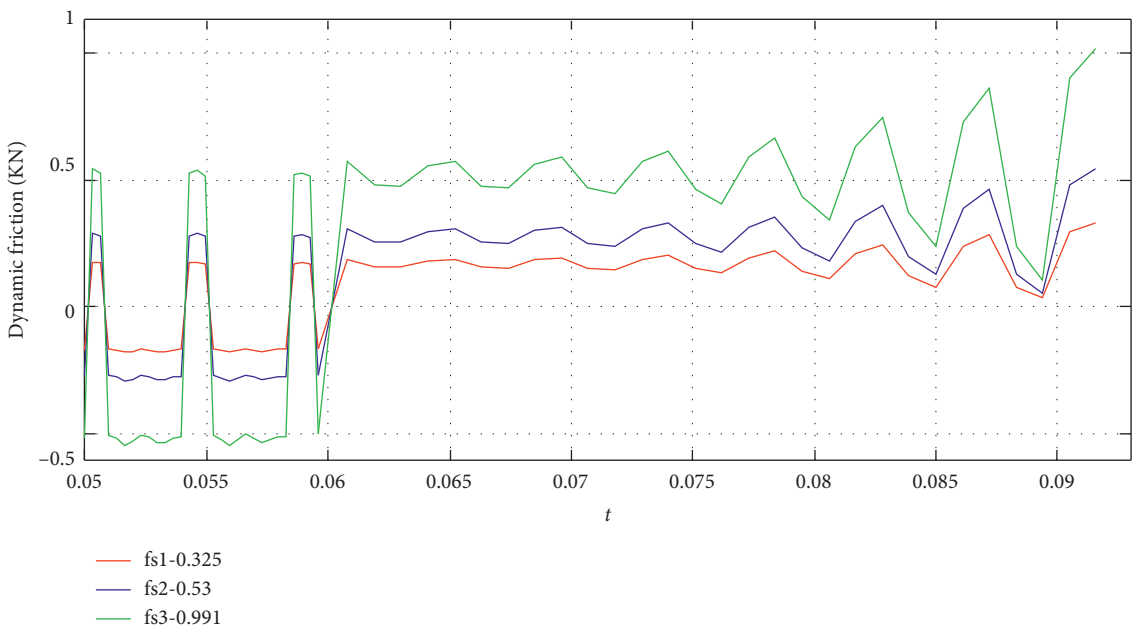

Figure 31: Dynamic friction from the smoothed Coulomb model.

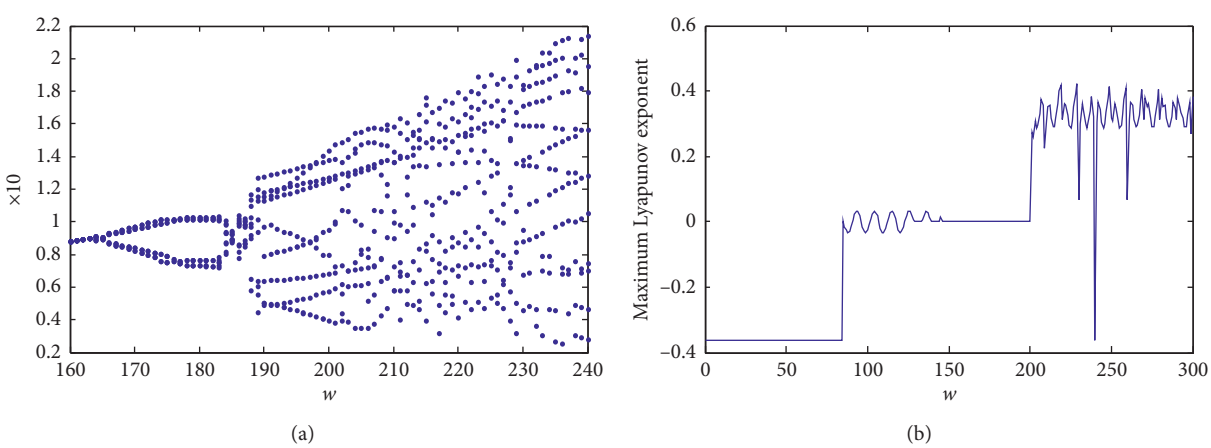

Figure 32: (a) Vibrational bifurcation diagram with the smoothed Coulomb model when $t \in [0.05 \;\; 0.0597]$. (b) Maximum Lyapunov exponent curve with the smoothed Coulomb model when $t \in [0.05 \;\; 0.0597]$.

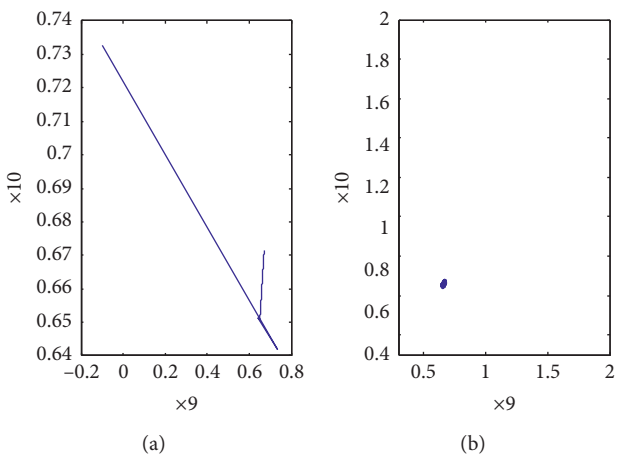

Figure 33: $\omega = 110$ and $k_w = 0$ with the smoothed Coulomb model when $t \in [0.05 \;\; 0.0597]$.

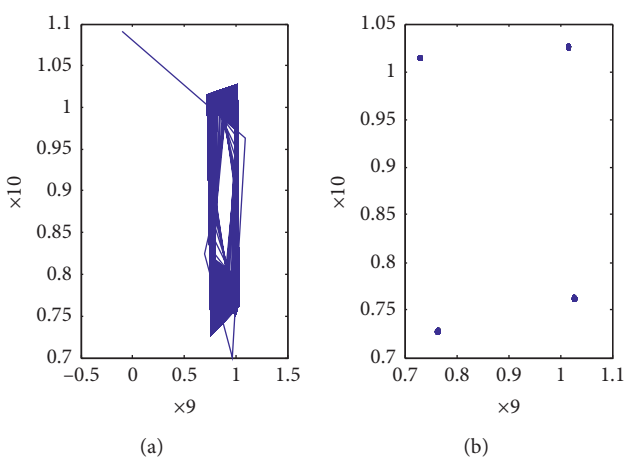

Figure 34: $\omega = 174$ and $k_w = 0$ with the smoothed Coulomb model when $t \in [0.05 \;\; 0.0597]$.

trajectories of the system at $\omega = 192$ are shown in Figure 35.

(5) When $0.05 < t < 0.0597$and $201 < \omega < 229$, corresponding phase trajectories of the system constitute a limit cycle. Poincare maps and corresponding phase trajectories of the system at $\omega = 210$ are shown in Figure 36.

(7) When $229 < \omega < 272$, the system has 13 periodic points. Poincare maps and corresponding phase trajectories of the system at $\omega = 230$ are shown in Figure 37.

(8) When $\omega > 272$, the system becomes divergent and uncontrollable. Poincare maps and corresponding phase trajectories of the system at $\omega = 273$ are shown in Figure 38.

From Figure 32(b), the maximum Lyapunov exponent is negative or fluctuates near zero when $\omega < 201$, indicating that the system is stable according to the Lyapunov theorem.

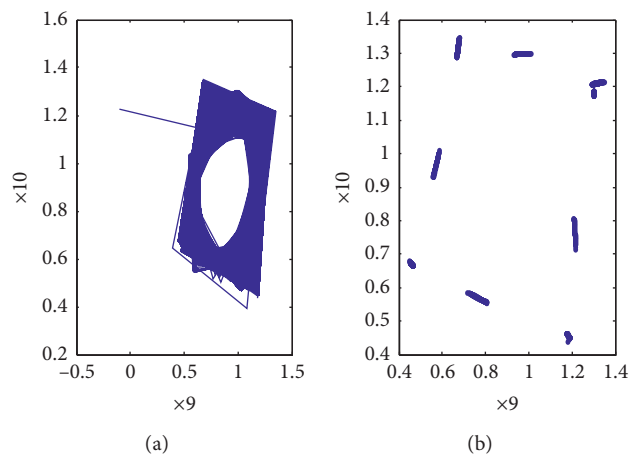

Figure 35: $\omega = 192$ and $k_w = 0$ with the smoothed Coulomb model when $t \in [0.05 \;\; 0.0597]$.

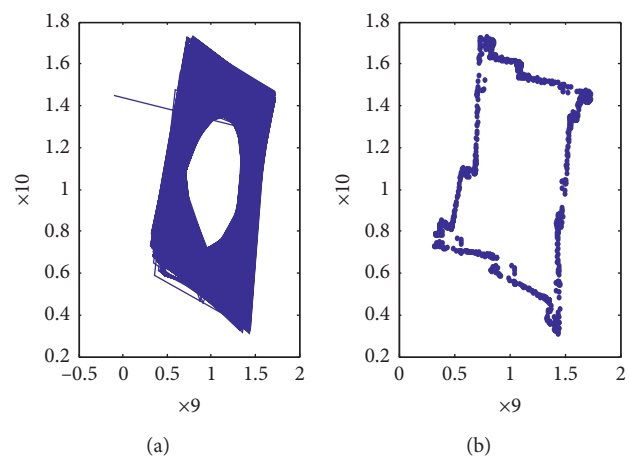

Figure 36: $\omega = 210$ and $k_w = 0$ with the smoothed Coulomb model when $t \in [0.05 \;\; 0.0597]$.

The maximum Lyapunov exponent is positive when $\omega > 201$, which indicates that the system exhibits chaos and becomes divergent and uncontrollable. In general, friction with the smoothed Coulomb model increases with an increase in tooth surface roughness because of the change of the nonlinear friction coefficient. Meanwhile, friction in the smoothed Coulomb model has nonperiodic and sharp fluctuations when $t > 0.0597$. Bifurcation diagrams, maximum Lyapunov exponents, phase diagrams, Poincare maps corresponding to Figure 31, and specific analyses are shown in Figures 39(a) and 39(b). Figure 39(a) shows the vibrational bifurcation diagram of the system using the smoothed Coulomb model to predict the time-varying friction coefficient when $0.0597 < t < 0.0921$, and the maximum Lyapunov diagram of the system is shown in Figure 39(b). From Figure 39(b), the maximum Lyapunov exponent is positive when $0.0597 < t < 0.0921$, which indicates that the system exhibits chaos and becomes divergent and uncontrollable. Here, the Poincare maps and corresponding phase trajectories of the system are omitted.

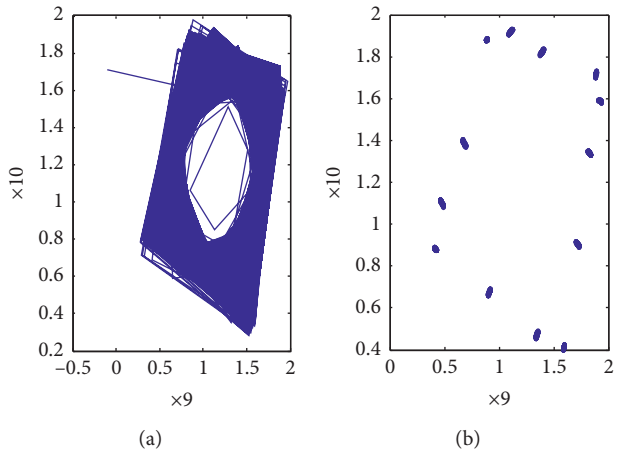

Figure 37: $\omega = 230$ and $k_w = 0$ with the smoothed Coulomb model when $t \in [0.05 \;\; 0.0597]$.

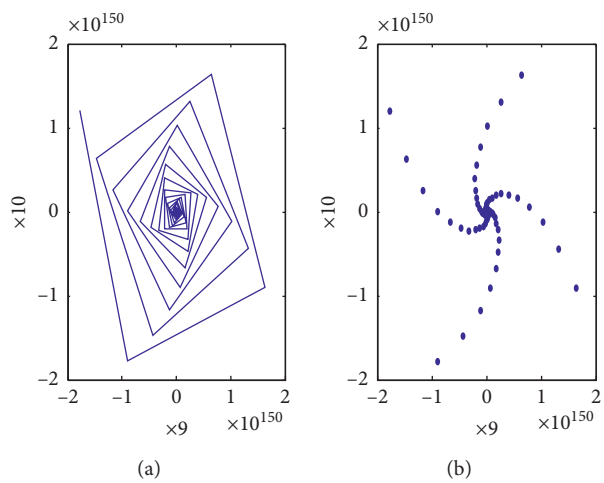

Figure 38: $\omega = 273$ and $k_w = 0$ with the smoothed Coulomb model when $t \in [0.05 \;\; 0.0597]$.

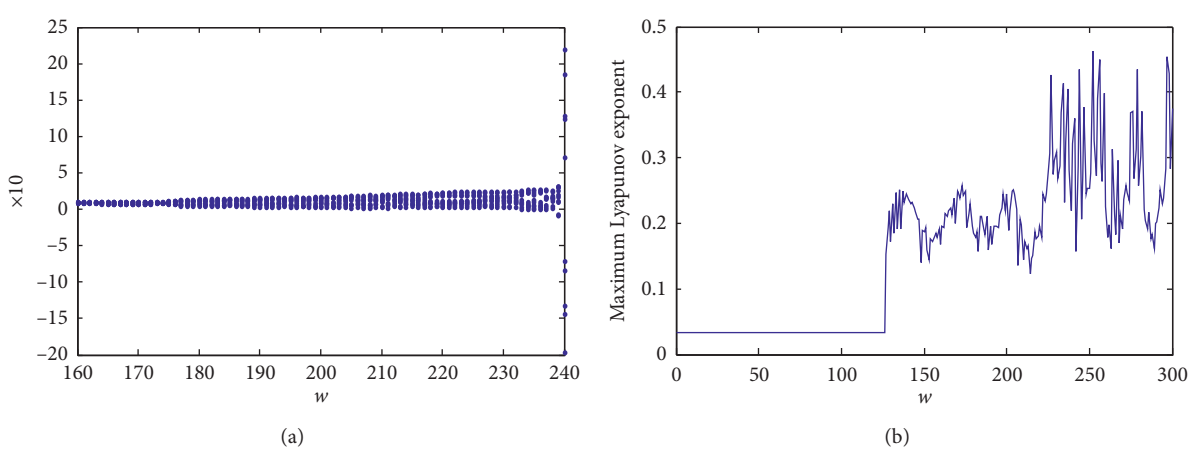

Figure 39: (a) Vibrational bifurcation diagram with the smoothed Coulomb model when $t \in [0.0597 \;\; 0.0921]$. (b) Maximum Lyapunov exponent curve with the smoothed Coulomb model when $t \in [0.0597 \;\; 0.0921]$.

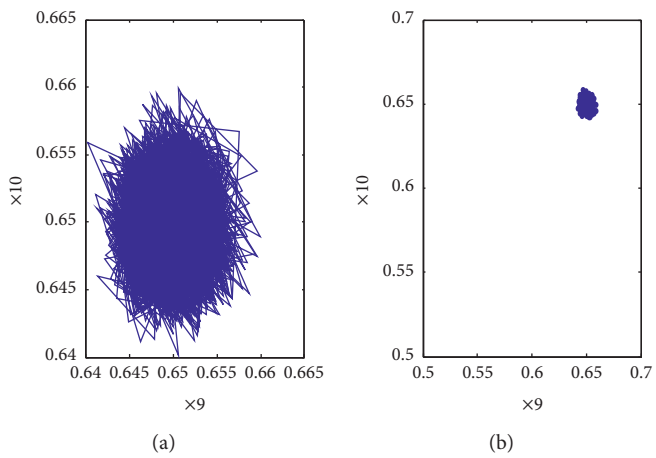

Figure 40: $\omega = 110$ with random perturbation.

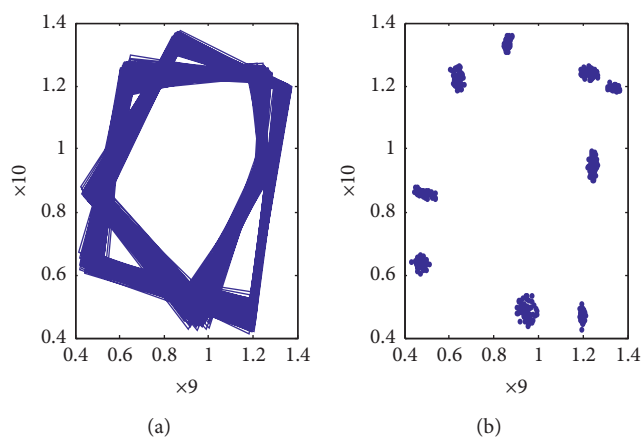

Figure 41: $\omega = 200$ with random perturbation.

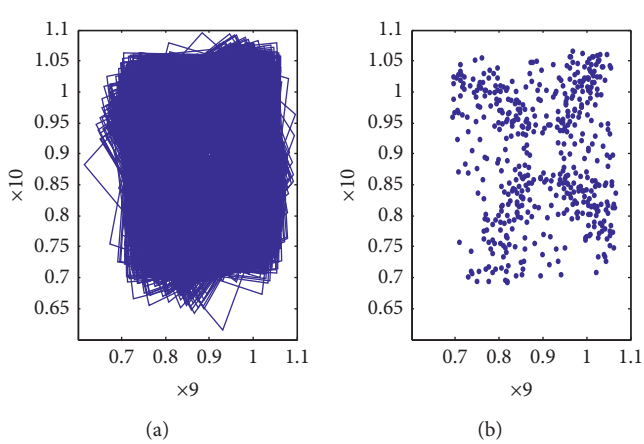

Figure 42: $\omega = 232$ with random perturbation.

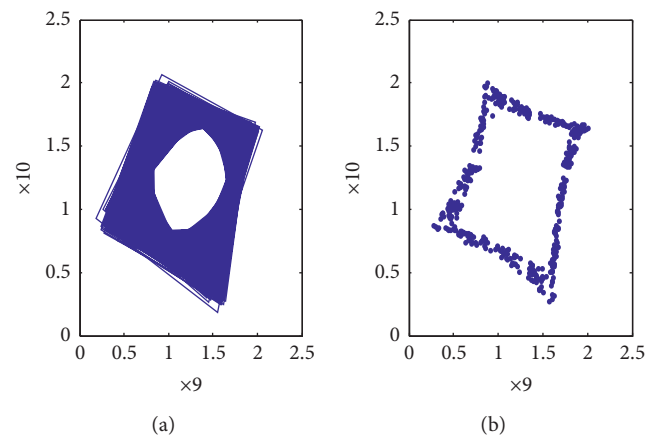

Figure 43: $\omega = 238$ with random perturbation.

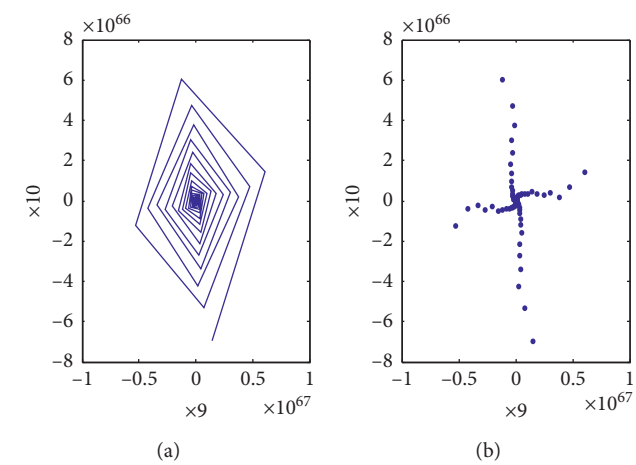

Figure 44: $\omega = 285$ with random Perturbation.

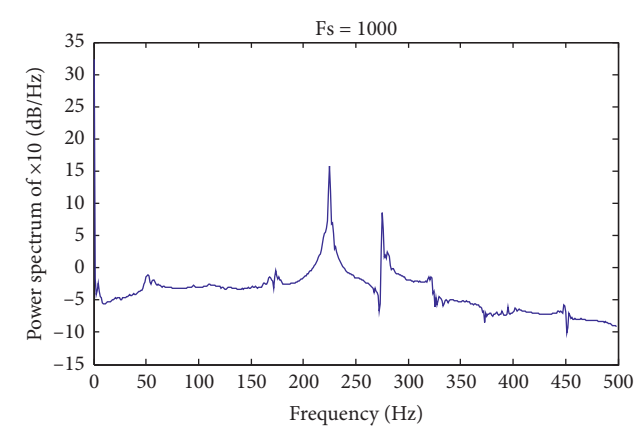

Figure 45: Power spectrum of $x_{10}$with random perturbation, $\omega = 175$.

3.4. Analysis of System with Random Perturbation. The nonlinear characteristics of a gear transmission system with random perturbation are analyzed as shown in Figures 40–48. The basic parameters are the same as those presented above, but some random perturbations are added here; these include δ_{px}, δ_{py}, δ_{gx}, δ_{gy}, δ_{ch1}, δ_{ch2}, δ_{ch3}, δ_{ε},

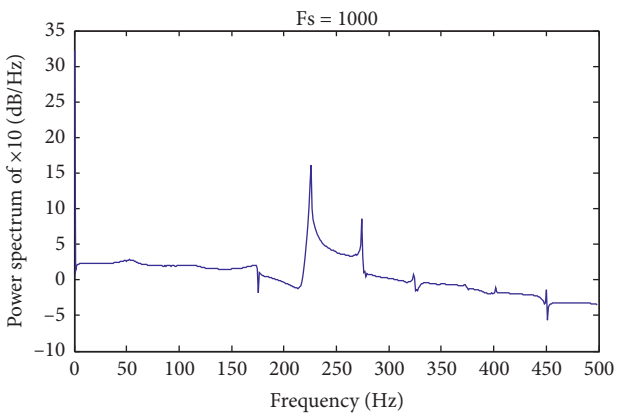

Figure 46: Power spectrum of x_{10} without perturbation, $\omega = 175$.

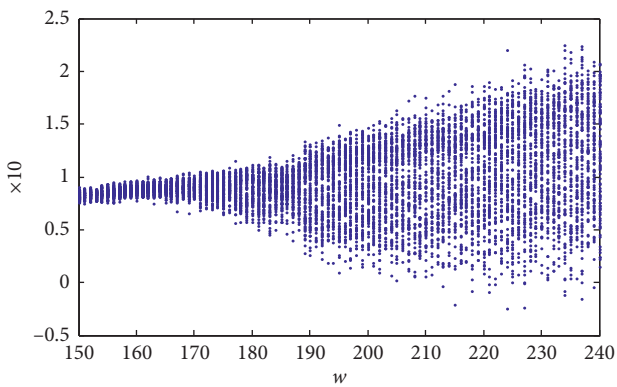

Figure 47: Vibrational bifurcation random diagram with $\delta_F^* \sim N(0, 0.01^2)$.

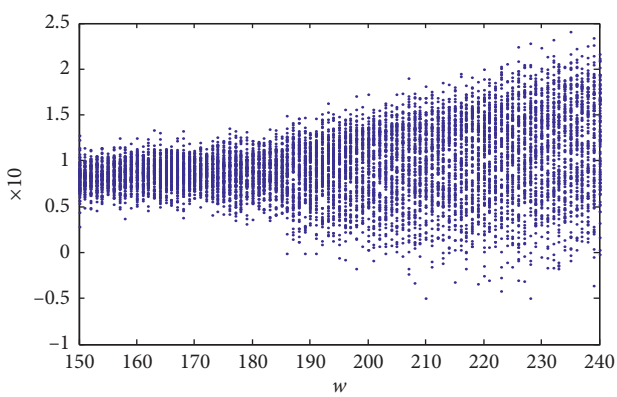

Figure 48: Vibrational bifurcation diagram with $\delta_F^* \sim N(0, 0.12^2)$.

$\delta_F^* \sim N(0, 0.001^2)$, and $\delta_{\omega h}^* \sim N(0, 0.00005^2)$. The Poincare maps and corresponding phase trajectories of the system with random perturbation are shown in Figures 40–44, in which the nonlinear characteristics of the gear transmission system with small random perturbation are basically consistent with the nonlinear characteristics of the system without random perturbation (as shown in Figures 7–12). The system with small random perturbations converges to some degree, but the system without random perturbations converges to a finite point. The power spectra in Figures 45 and 46 were generated with a sampling frequency of 1000.

The trend of the power spectrum of x_{10} with and without random perturbation is almost identical, but the fluctuation of the power spectrum of x_{10} with random perturbation is greater than that without random perturbation.

The vibrational bifurcation diagrams of the system with $\delta_F^* \sim N(0, 0.01^2)$, $\delta_F^* \sim N(0, 0.12^2)$ are shown in Figures 47 and 48. With the increase of δ_F^*, the dynamic characteristics of the system change from Figure 47 to 48. When δ_F^* increases to the extent that $\delta_F^* \sim N(0, 0.12^2)$, the bifurcation of the system disappears completely and the system becomes uncontrollable.

4. Conclusions

This study investigates the nonlinear characteristics of a gear transmission system in a braiding machine experiencing multiple excitation factors. The well-known radial braiding machine with one layer was used to investigate the nonlinear characteristics of the gear transmission system. The results show that the nonlinear characteristics of the gear transmission system under the influence of multiple excitation factors were in accordance with the principles of practical engineering.

In conclusion, this research on the nonlinear characteristics of the gear transmission system in a braiding machine is helpful for engineers engaged in future design of this well-known machine. Our findings include the following:

(1) According to the bifurcation diagram of the system without random perturbation, the system exhibits chaos when $\omega > 213$. Therefore, ω must be controlled so $\omega < 213$, that is, the speed is 25561.25 r/s. If factors such as yarn tension and safety are taken into account, the safe speed in this braiding machine might be under about 302.5r/s, or 1.815×10^3 r/min.

(2) k_w has a great influence on the nonlinear characteristics of the gear transmission system. With an increase in k_w, e.g., with $k_w \geq 0.32$, the system of the radial braiding machine with one layer always exhibits chaos. Therefore, k_w must be controlled so that $k_w < 0.32$.

(3) Friction on the tooth surface has a large influence on the nonlinear characteristics of the gear transmission system. The Coulomb model and the smoothed Coulomb model are used to predict the time-varying friction coefficient. In general, friction on the tooth surface increases with increasing tooth surface roughness because of the change in the nonlinear friction coefficient. The system always exhibits chaos when $t > 0.0581$ with the Coulomb model used to predict the time-varying friction coefficient. Meanwhile, the system always exhibits chaos when $t > 0.0597$, and the smoothed Coulomb model is used to predict the time-varying friction coefficient.

(4) The system with small random perturbations converges to some degree, and the system without

random perturbation converges to a finite point. However, the dynamic characteristics of the system have not changed. The increase of some certain perturbations does lead to changes in the dynamic characteristics of the system. When δ_F^* increases to the extent that $\delta_F^* \sim N(0, 0.12^2)$, the bifurcation of the system disappears completely and the system becomes uncontrollable.

In this paper, we analyze nonlinear dynamic characteristics of a gear transmission system in a braiding machine and only consider disturbance of yarn tension, transmission error, time-varying friction, and contact temperature because of the time limit. However, many other factors have an important influence on nonlinear dynamic characteristics of a gear transmission system. Future research on the influence of other excitation factors operating on the gear transmission system in a braiding machine would be of value.

Data Availability

The data used to support the findings of this study are available from the corresponding author upon request.

Conflicts of Interest

The authors declare no potential conflicts of interest with respect to the research, authorship, and/or publication of this article.

Acknowledgments

This project was supported by the Special Fund of Scientific and Technological Achievements Transformation in Jiangsu Province (grant no. BA2018061), the Program of Jiangsu Innovative Talent (grant no. 20171122), the Fundamental Research Funds for the Central Universities, and Graduate Student Innovation Fund of Donghua University (grant number CUSF-DH-D-2019097).

References

[1] G. Ma, D. J. Branscomb, and D. G. Beale, "Modeling of the tensioning system on a braiding machine carrier," *Mechanism and Machine Theory*, vol. 47, pp. 46–61, 2012.

[2] G. Guyader, A. Gabor, and P. Hamelin, "Analysis of 2D and 3D circular braiding processes: modeling the interaction between the process parameters and the pre-form architecture," *Mechanism and Machine Theory*, vol. 69, pp. 90–104, 2013.

[3] J. Hajrasouliha, R. J. Nedoushan, M. Sheikhzadeh, W. Na, and W. R. Yu, "Theoretical and experimental study of braid pattern in mandrels with arbitrary cross-sections," *Journal of Composite Materials*, vol. 52, no. 29, pp. 4009–4022, 2018.

[4] Y. Shen and D. J. Branscomb, "A general approach to fast prototype the topology of braided structures," *International Journal Engineering Science*, vol. 131, pp. 40–60, 2018.

[5] T. Wehrkamp-Richter, R. Hinterhölzl, and S. T. Pinho, "Damage and failure of triaxial braided composites under multi-axial stress states," *Composites Science and Technology*, vol. 150, pp. 32–44, 2017.

[6] E. E. Swery, T. Hans, M. Bultez et al., "Complete simulation process chain for the manufacturing of braided composite parts," *Composites Part A: Applied Science and Manufacturing*, vol. 102, pp. 378–390, 2017.

[7] Y. Zhang, Z. Meng, and Y. Sun, "Dynamic modeling and chaotic analysis of gear transmission system in a braiding machine with or without random perturbation," *Shock and Vibration*, vol. 2016, Article ID 8457645, 12 pages, 2016.

[8] A. Kahraman and R. Singh, "Non-linear dynamics of a spur gear pair," *Journal of Sound and Vibration*, vol. 142, no. 1, pp. 49–75, 1990.

[9] A. Kahraman and R. Singh, "Interactions between time-varying mesh stiffness and clearance non-linearities in a geared system," *Journal of Sound and Vibration*, vol. 146, no. 1, pp. 135–156, 1991.

[10] M. Vaishya and R. Singh, "Analysis of periodically varying gear mesh systems with coulomb friction using Floquet theory," *Journal of Sound and Vibration*, vol. 243, no. 3, pp. 525–545, 2001.

[11] A. C. J. Luo, "Past current and future on nonlinear dynamics and noise origins of non-smooth gear transmission dynamic systems," in *Proceedings of the IEEE Intelligent Vehicles Symposium*, Las Vegas, NV, USA, June 2005.

[12] S. He, T. Rook, and R. Singh, "Construction of semianalytical solutions to spur gear dynamics given periodic mesh stiffness and sliding friction functions," *Journal of Mechanical Design*, vol. 130, no. 12, pp. 1226011–1226019, 2008.

[13] G. Liu and R. G. Parker, "Dynamic modeling and analysis of tooth profile modification for multi-mesh gear vibration," *Journal of Mechanical Design*, vol. 130, no. 12, pp. 1214021–12140213, 2008.

[14] C.-J. Chang-Jian, "Bifurcation and chaos analysis of the porous squeeze film damper mounted gear-bearing system," *Computers & Mathematics with Applications*, vol. 64, no. 5, pp. 798–812, 2012.

[15] S. Li and A. Kahraman, "A transient mixed elastohydrodynamic lubrication model for spur gear pairs," *Journal of Tribology*, vol. 132, no. 6, pp. 011501–011509, 2010.

[16] K. J. Huang, M. R. Wu, and J. T. Tseng, "Dynamic analyses of gear pairs incorporating the effect of time-varying lubrication damping," *Journal of Vibration and Control*, vol. 17, no. 3, pp. 355–363, 2011.

[17] T. Eritenel and R. G. Parker, "Three-dimensional nonlinear vibration of gear pairs," *Journal of Sound and Vibration*, vol. 331, no. 15, pp. 3628–3648, 2012.

[18] Y. Cui, Z. Liu, and Y. Wang, "Nonlinear dynamic of a geared rotor system with nonlinear oil film force and nonlinear mesh force," *Journal of Vibration and Acoustics*, vol. 134, no. 4, pp. 041001–041008, 2012.

[19] Z. G. Chen, Y. M. Shao, and T. C. Lim, "Non-linear dynamic simulation of gear response under the idling condition," *International Journal of Automotive Technology*, vol. 13, no. 4, pp. 541–552, 2012.

[20] S. Baguet and G. Jacquenot, "Nonlinear couplings in a gear-shaft-bearing system," *Mechanism and Machine Theory*, vol. 45, no. 12, pp. 1777–1796, 2010.

[21] S. Li and A. Kahraman, "A tribo-dynamic model of a spur gear pair," *Journal of Sound and Vibration*, vol. 332, no. 20, pp. 4963–4978, 2013.

[22] J. Wei, Q.-C. Sun, W. Sun et al., "Dynamic analysis and effects of nonlinear factors of a gear transmission system for high speed locomotive," *Journal of Vibration and Shock*, vol. 31, no. 17, pp. 38–43, 2012.

[23] H.-D. Gao, Y.-D. Zhang, Q. Wu et al., "Nonlinear dynamic characteristics of a confluence transmission geared rotor

bearing system," *Journal of Vibration and Shock*, vol. 32, no. 8, pp. 105–113, 2013.

[24] H.-B. Zhang, R. Wang, Z.-K. Chen et al., "Nonlinear dynamic analysis of a gear-rotor system with coupled multi-clearance," *Journal of Vibration and Shock*, vol. 34, no. 8, pp. 144–150, 2015.

[25] G. Xiang-Feng, "*Research on the dynamic characteristics of the single stage spur gear system considering temperature factor*," M.S. thesis, Lanzhou Jiaotong University, Lanzhou, China, 2016.

[26] J. Zhang, *Simulation and experimental research on gear transmission dynamics with various excitation factors*, M.S. thesis, Chongqing University, Sichuan, China, 2012.

[27] C. Duan and R. Singh, "Super-harmonics in a torsional system with dry friction path subject to harmonic excitation under a mean torque," *Journal of Sound and Vibration*, vol. 285, no. 4-5, pp. 803–834, 2005.